# Electrical properties of epitaxial yttrium iron garnet ultrathin films at high temperatures

N. Thiery,[1] V. V. Naletov,[1,2] L. Vila,[1] A. Marty,[1] A. Brenac,[1] J.-F. Jacquot,[1] G. de Loubens,[3] M. Viret,[3] A. Anane,[4] V. Cros,[4] J. Ben Youssef,[5] N. Beaulieu,[5] V. E. Demidov,[6] B. Divinskiy,[6] S. O. Demokritov,[6,7] and O. Klein[1,*]

[1]*SPINTEC, CEA-Grenoble, CNRS and Université Grenoble Alpes, 38054 Grenoble, France*
[2]*Institute of Physics, Kazan Federal University, Kazan 420008, Russian Federation*
[3]*SPEC, CEA-Saclay, CNRS, Université Paris-Saclay, 91191 Gif-sur-Yvette, France*
[4]*Unité Mixte de Physique CNRS, Thales, Université Paris-Saclay, 91767 Palaiseau, France*
[5]*LabSTICC, CNRS, Université de Bretagne Occidentale, 29238 Brest, France*
[6]*Department of Physics, University of Muenster, 48149 Muenster, Germany*
[7]*Institute of Metal Physics, Ural Division of RAS, Yekaterinburg 620041, Russian Federation*

(Received 20 September 2017; revised manuscript received 22 January 2018; published 26 February 2018)

We report a study on the electrical properties of 19-nm-thick yttrium iron garnet (YIG) films grown by liquid phase epitaxy on gadolinium gallium garnet single crystal. The electrical conductivity and Hall coefficient are measured in the high-temperature range [300,400] K using a Van der Pauw four-point probe technique. We find that the electrical resistivity decreases exponentially with increasing temperature following an activated behavior corresponding to a band gap of $E_g \approx 2$ eV. It drops to values about $5 \times 10^3\ \Omega\,\mathrm{cm}$ at $T = 400$ K, thus indicating that epitaxial YIG ultrathin films behave as large gap semiconductors. We also infer the Hall mobility, which is found to be positive ($p$ type) at 5 $\mathrm{cm^2\,V^{-1}\,sec^{-1}}$ and almost independent of temperature. We discuss the consequence for nonlocal spin transport experiments performed on YIG at room temperature and demonstrate the existence of electrical offset voltages to be disentangled from pure spin effects.

DOI: 10.1103/PhysRevB.97.064422

## I. INTRODUCTION

The recent discovery that spin-orbit effects [1–4] could allow to generate or to detect pure spin currents circulating in an adjacent magnetic layer has triggered a renewed interest for magnon transport in magnetic oxides, and in particular yttrium iron garnet, $Y_3Fe_5O_{12}$ (YIG) [2,5–18], the material with the lowest known magnetic damping in nature. It confers to YIG the unique ability to propagate the spin information on the largest possible distance. Moreover, in electrical insulators, all effects associated with electrical transport are absent, which simplifies greatly the interpretation of the measurements.

The latest studies on the magnon transport properties of YIG concentrate on the strong out-of-equilibrium regime where large spin currents are induced in the YIG either by spin transfer torque [17,18] or by temperature gradients [19,20]. When performed at room temperature, this involves heating the YIG material well above 300 K. One concern is the issue of whether YIG could become an electrical conductor at such high temperatures. Indeed, it is known [21–26] that the electrical resistivity of doped YIG could decrease by several orders of magnitude with increasing temperature due to the presence of impurities. In the case of ultrathin films, defects could come from the growth method or from the two interfaces and potentially lead to a spurious charge conduction channel when heated well above 300 K. In order to clarify this point, we propose to investigate the evolution of the electrical properties of single crystalline YIG ultrathin films in the temperature range [300,400] K.

Before describing the experimental procedure, we would like to recall that YIG is a ferrimagnet, which has an uncompensated magnetic moment on the $Fe^{3+}$ ions, found on octahedral and tetrahedral coordinate sites, both coupled by superexchange. Studies on Ca- and Si-doped YIG [21] have established that $Fe^{2+}$ and $Fe^{4+}$ ions are formed if tetravalent or respectively divalent impurities are added to the YIG, which could then lead to an electrical conduction via the charge transfer mechanism, respectively, of $p$ and $n$ type. In that case, the doped YIG behaves as a large gap semiconductor with a charge conductivity following an activation mechanism. At the present stage, different studies disagree about the microscopic mechanism at play for the electronic conduction inside doped YIG, whether it follows a localized hopping model, through a small polaron conduction [25] or rather a band model, through a large polaron conduction [21]. It is also known that the value of the magnetic damping coefficient of YIG is very sensitive to the doping level. This is because the charge transfer between the mixed valence iron ions is associated to a potent magnetic relaxation process, known as the valence exchange relaxation [27]. So far, this mechanism activated by impurities, appears in the form of a large enhancement of the magnetic damping, usually around liquid nitrogen temperature, where the fluctuation rate of the charge transfer matches the Larmor frequency. This effect is usually minimized by growing YIG crystals from ultrapure materials. Quite remarkably, YIG can usually be synthesized in large volume in the form of a single crystal with almost no atomic disorder. It has been reported that the resistivity of bulk ultrapure YIG can be as large as $10^{12}\ \Omega\,\mathrm{cm}$ at room temperature [22].

*Corresponding author: oklein@cea.fr

 

But, as explained in Introduction, recent interest on spin transfer effects in YIG have required an effort to develop high quality YIG material in the form of ultrathin (below 20 nm) films (thickness should be compared here relatively to the YIG unit cell, which is 1.238 nm). This is because spin transfer is an interfacial phenomenon and consequently its efficiency increases with decreasing thickness of the magnetic layer. Three growth techniques have, so far, allowed to produce good quality ultrathin YIG films: sputtering [28–30], pulsed laser deposition [8,31–33], and liquid phase epitaxy (LPE) [7,18,34]. These films are usually grown on gadolinium gallium garnet, $Gd_3Ga_5O_{12}$ (GGG) substrates, which provides the necessary lattice matching to achieve epitaxial growth. For all these, three growth processes, the quality of the YIG films deteriorates as the film thickness decreases [8,34]. This deterioration is an inherent consequence of an increasing surface to volume ratio, which substantially enhances the possibilities for defects and impurities to be introduced into the YIG, through the two surfaces (contamination, intermixing of the species at the surface, or unrelaxed strains in the film thickness), which leads to lower saturation magnetization and an out-of-plane anisotropy often accompanied by an increase of the coercive field.

So far, the highest thin film quality (smallest combination of low magnetic damping parameter, low inhomogeneous broadening, and film thickness below 20 nm) have been reported for films grown by the LPE technique, an extension of the flux method. Garnets have a noncongruent melting phase and can only be prepared in the form of single crystals once dissolved in a solvent. The solvent used is usually a mixture of different oxide elements, mainly PbO and $B_2O_3$, which can eventually enter as impurities in the flux growth. The molten mixture is confined in a platinum crucible (inert with respect to the oxides) placed in an epitaxy furnace above the saturation temperature, defined as the temperature at which the growth rate is zero. Subsequently, the GGG substrate with crystallographic orientation (111) is immersed in the bath. Optimization of the growth process parameters is achieved by studying the dependencies of the depositing conditions on the structural, morphological, and magnetic properties. The key to very good growth is to keep the solution perfectly homogeneous and the growth rate very slow. The main problem is the difficulty in developing a recipe leading to YIG films homogeneous in both thickness and composition. Indeed, for very thin layers, the role of the transition layer is essential (chemical composition) and requires a control of the chemical elements composing it. The influence of this transition layer on the different contributions to the linewidth is important. The YIG films that we have developed from LPE growth technique have the following characteristics: perfect epitaxy (difference of matching parameter with the substrate is null); saturation magnetization almost equal to that of the bulk ($4\pi M_s$ of our 19 nm YIG films is about 1.7 kG); very low magnetic relaxation (damping coefficient less than or equal than $3.2 \times 10^{-4}$); no planar anisotropy and very weak coercive field ($H_c < 3$ Oe); very low roughness (3 $Å_{rms}$).

TABLE I. Summary of the physical properties of the YIG thin film (YDPB9) used in this study.

| $t_{YIG}$ (nm) | $4\pi M_s$ (G) | $\alpha_{YIG}$ | $\Delta H_0$ (Oe) | $\gamma$ (rad s$^{-1}$ G$^{-1}$) |
|---|---|---|---|---|
| 19 | $1.67 \times 10^3$ | $3.2 \times 10^{-4}$ | 2.5 | $1.79 \times 10^7$ |

## II. ELECTRICAL PROPERTIES OF BARE YIG THIN FILMS

In the following, we will concentrate on the electronic properties of LPE grown YIG thin films of thickness $t_{YIG} = 19$ nm. The dynamical characteristics of these films are summarized in Table I. A $1 \times 1$ mm$^2$ square slab of YIG is extracted from the batch and connected along the four corners using Al wire bonding. The measurements are performed inside a homemade cryostat regulated in temperature by a flow of helium gas. To characterize the slab we use the van der Pauw four probes method [35], which is typically used to measure the sheet resistance of homogeneous semiconductor films. It allows to eliminate measurement errors associated with the exact shape of the sample. The four points are arranged in a clockwise order around the positive field normal shown schematically inside Fig. 1(a). Because of YIG high impedance, we use a Keithley 2636B source-measurement unit in order to draw very little current (subnanoamper range) inside the film. In our analysis, the GGG substrate will be considered a good insulator (resistivity $> 10^{15}$ Ω cm) [22] and its electrical conductivity will be ignored.

Our measurements are performed at high temperature in the range [300,400] K and for different magnetic fields in the range [0,5] T applied normally to the sample surface. The temperature range explored is still well below the Curie temperature of YIG, which is $T_C = 562$ K. We first extract the sheet resistance $R_s$, which consists in measuring all possible combinations of the cross-resistance between opposite edges. From the van der Pauw expression, one can extract $R_s$, whose minimum lays in the couple of GΩ range at the highest temperature. From the sheet resistance, we compute the resistivity $\rho = R_s t_{YIG}$. Figure 1 shows the resistivity as a function of temperature.

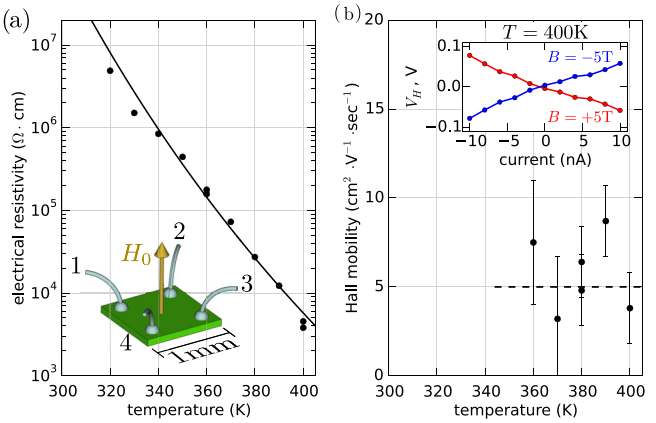


FIG. 1. Temperature dependence of (a) the electrical resistivity and (b) Hall mobility of 19-nm-thick YIG films grown by LPE determined by a Van der Pauw four-point probe technique (see inset). The solid line in (a) is a fit with an activated behavior $\exp[E_g/(2k_BT)]$, where $E_g \approx 2$ eV. The inset in (b) shows the Hall voltage drop $V_{i+1,i+3}$ when the current is injected between $I_{i,i+2}$, where $i$ is the contact number modulo 4.

The first remarkable feature is that the resistivity of YIG at 400 K drops to about $5 \times 10^3$ Ω cm. Plotting the data on a semilogarithmic scale helps to show that the resistivity decay follows an exponential behavior. Fitting a linear slope through the data plotted as a function of $1/T$ (in Fig. 1, the data are shown as a function of $T$), we infer a band-gap energy of about $E_g \approx 2$ eV, which is about 1 eV lower than the expected band gap of pure YIG in bulk form.

Next, we characterize the Hall conductance of our sample. For this, we now circulate the electrical current along the diagonals $I_{i,i+2}$ and measure the voltage drop along the opposite contacts $V_{i+1,i+3}$. Here, $i$ is the contact number modulo 4, where the subscript notation is ordered according to the connections to the high/low binding posts of the current source and voltmeter. The inset of Fig. 1(b) shows the voltage drop measured at 400 K in the presence of a normal magnetic field of 5 T. To eliminate the resistivity offset, we have worked out the difference of the voltages for positive and negative magnetic fields. In our measurement geometry, the polarity of the Hall voltage is opposite to the magnetic field direction. It implies that the trajectories of the charge carriers are deflected in the opposite direction to the current in the electromagnet, or in other words that the YIG behaves as a $p$-type conductor. Quantitatively, the full variation of the Hall voltage is about 0.12 V at 10 nA when the field is changed by $H_0 = \pm 5$ T at 400 K, where the YIG resistivity is $\rho = 5 \times 10^3$ Ω cm. This corresponds to a carrier mobility for the holes of about $\mu_H \approx 5 \pm 3$ cm$^2$ V$^{-1}$ sec$^{-1}$. We have repeated the measurement for other temperatures. The measurement at lower temperature is difficult for two reasons. The first one is the limited voltage range of the sourcemeter, which decreases the upper current limit that could be injected in the YIG. Another consequence of the large resistivity is the associated increase of the time constant for charging effects. This increases substantially the dwell time necessary before taking a measurement. Because of these difficulties, we have limited the measurement range to 40 K below the maximum temperature. Although the error bars of our measurement are large, the result suggests that the temperature dependence of the mobility as a function of temperature is small [36] indicating that most of the change in the resistivity comes from a variation of the electronic density and not of the scattering time. Such behavior is compatible with what has been found previously in Ca-doped YIG ($p$-type) and this observation is used as a signature that charge carriers are provided by large polarons [21]. Our study does not conclude if the electrical conduction occurs in the bulk or if this is a surface effect. This important question shall be determined in future studies by monitoring the change in the electrical properties as a function of the YIG thickness.

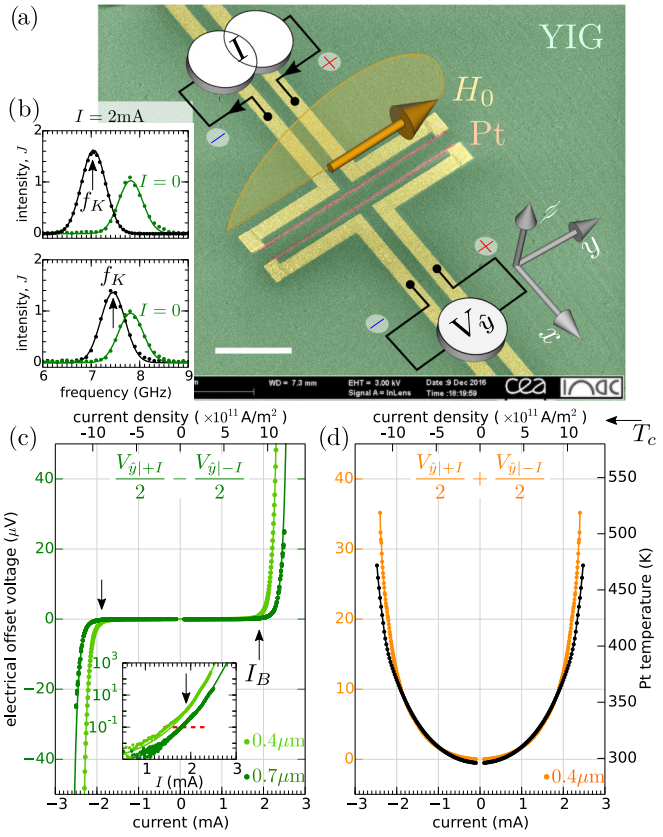


FIG. 2. Current dependence of the electrical offset voltage $V_{\hat{y}}$ in nonlocal transport devices performed at room temperature. The YIG magnetization is set along the $y$ direction by an external in-plane magnetic field biased at $H_0 = 2$ kOe. One monitors here the voltage along one wire as a current flows through a second wire separated by a variable gap (0.4 or 0.7 $\mu$m). (a) A microscopy image showing two Pt stripes aligned along the $y$ direction (red) (the scale bar is 10 $\mu$m). The polarity of the current source and voltmeter are specified. (b) A direct monitoring through microfocus Brillouin light scattering of the value of YIG saturation magnetization (temperature sensitive) underneath the Pt injector ($i$) and the Pt detector ($d$) here separated by a gap of 0.7 $\mu$m. The maximum of the curve indicate the position of the Kittel frequency (see arrows). Shifts produced by Joule heating at $I = 2$ mA (black) are shown relatively to the results at $I = 0$ (green). (c) and (d) show the current variation of the offset voltage, here decomposed in two contributions: (c) $(V_{\hat{y}|+I} - V_{\hat{y}|-I})/2$, odd in current (green), and (d) $(V_{\hat{y}|+I} + V_{\hat{y}|-I})/2$, even in current (orange). The black curve in (d) shows the increase of relative resistance of the Pt used as a temperature sensor. The results in (c) are shown for two different gap separation between the Pt wires. The solid line in (b) is a fit with an exponential increase $\exp[-E_g/(2k_BT)]$, where $E_g \approx 2$ eV. The inset is a zoom of the data and shown on a semilogarithmic scale. The arrow at $I_B = 2$ mA indicates the threshold current above which the Ohmic losses start to reach the 100 nV range.

## III. IN-PLANE OFFSET VOLTAGE IN NONLOCAL YIG|Pt DEVICES: $M_s \parallel \hat{y}$

Next, we investigate the implications of these electrical properties for nonlocal spin transport experiments [37] performed at room temperature and in air, where one monitors the transport properties between two parallel Pt wires [colored in red in Fig. 2(a)] deposited on top of YIG. More precisely, one measures the voltage along one wire (the detector) as a current flows through a second wire (the injector). Figure 2(a) shows a microscopy image of the electrode pattern on top of the YIG. For the sake of clarity, we define a Cartesian frame where the $\hat{y}$ direction is set parallel to the wire and the $\hat{z}$ direction represents the out-of-plane orientation. For the lateral device series used herein, the Pt wires are 7-nm thick, 300-nm wide, and 30-$\mu$m long. Since different Pt wires (thickness and

length) have been deposited between different samples [18], comparison of the results should be done by juxtaposing data obtained with identical current densities (provided in the upper scale). The total resistance of the Pt wire at room temperature is $R_0 = 3.9$ k$\Omega$, corresponding to a Pt resistivity of 27.3 $\mu\Omega$ cm. The analysis below will concentrate on two devices, with two Pt wires separated by a gap of either 0.7 or 0.4 $\mu$m, respectively. We emphasize though that these measurements have been performed on several other devices patterned on two different LPE YIG film batches [18] of about similar thickness. In the following, we shall explicitly clarify the effects, that are generic to the YIG films.

In the measurements, the current is injected in the device only during 10-ms pulses using a 10% duty cycle (cf. Appendix for more details). This pulse method is very important in order to limit heating of the YIG and substrate. The increase of resistance $R_I$ of the Pt wire is monitored during the pulse sequence. The result is shown in Fig. 2(c) (right axis), where we have plotted $\kappa_{\rm Pt}(R_I - R_0)/R_0$ as a function of the current $I$, with the coefficient $\kappa_{\rm Pt} = 254$ K specific to Pt [38]. The result is shown in Fig. 2(d) using black dots. For information purposes, we have also marked on the plot the position of the Curie temperature $T_C$. We have performed on the device with a gap of $d = 0.7$ $\mu$m, microfocus Brillouin light scattering ($\mu$-BLS) in the GHz energy range. The spectral distribution of light intensity measured either by focusing the light beam under the injector ($i$) or detector ($d$) Pt wire is shown in Fig. 2(b). The $\mu$-BLS spectrum is first measured at $I = \pm 0$ mA for calibration purpose. The spectral distribution is then measured at $I = \pm 2$ mA (i.e., $9.5 \times 10^{11}$ A/m$^2$) while the field is set to $H_0 = +2$ kOe along the $\hat{y}$ direction. The spectrum shifts to lower frequencies, due to a reduction of the saturation magnetization $M_s$ caused by the excitation of magnons. Since the frequency of the maximum in the spectrum [arrows in Fig. 2(b)] coincides with the FMR frequency, we can calculate $M_s$ from the experimental data by using the Kittel formula. The quantity $\Delta M_s = M_s(0) - M_s(I)$, where $M_s(0)$ is the effective magnetization at $I = 0$, characterizes the total number of magnons created due to the current flowing in Pt. Comparing these values at the (i) and (d) position allows to estimate the decrease of saturation magnetization under the injector ($-290$ G) and the detector ($-110$ G). If one uses the fact that YIG magnetization decreases by 4G/°C in this temperature range, we find that at $I = 2$ mA the temperature of the YIG underneath the injector has increased by $+73$ °C, while the temperature of the YIG underneath the detector has increased by $+27$ °C. This result thus suggests that the local YIG temperature is identical to that of the Pt (i.e., negligible Kapitza resistance).

One can then use these findings to estimate the temperature effects on the electrical properties. At $I = 2$ mA, which corresponds to a current density of about $10^{12}$ A/m$^2$ in the Pt injector wire, the temperature of the Pt increases to about 370 K during the pulse. At this temperature, the YIG resistivity drops into the sub-$10^5$ $\Omega$ cm range according to Fig. 1(a), which corresponds to a sheet resistance of about 50 G$\Omega$. Considering now the lateral aspect ratio of the device, this amounts to an electrical resistance of YIG of the order of the G$\Omega$ between the two wires. The leakage current inside the Pt detector wire, whose impedance is about six orders of magnitude smaller than that of YIG, starts thus to reach the nanoamper range. This is comparable to contributions from other effects stemming from spin currents flowing from injector to detector, either due to temperature gradients or magnon emission and propagation and transduced to an electrical current in the Pt by inverse spin Hall effects (ISHE).

To resolve this effect in our lateral device, we propose to measure the nonlocal voltage with the magnetization set precisely parallel to the Pt wire ($\hat{y}$ direction). This configuration switches off completely any sensitivity to spin conduction. To align the magnetization with the wire, we use an external in-plane magnetic field of 2 kOe as shown in Fig. 2. The induced offset voltage is decomposed in two contributions: (b) one $(V_{\hat{y}|+I} - V_{\hat{y}|-I})/2$, which is odd in current (green) and the other (c) $(V_{\hat{y}|+I} + V_{\hat{y}|-I})/2$, which is even in current (orange).

We first concentrate on the odd contribution of the offset shown in green in Fig. 2(c). The result is shown for two different nonlocal devices, where the two Pt wires are separated by two different gaps respectively 0.4 and 0.7 $\mu$m. On a linear voltage scale set to the microvolt range, we observe that the odd offset increases abruptly above $I_B = 2$ mA on the 0.7 $\mu$m device (corresponding to a YIG temperature of 370 K). This abrupt rise is shifted to lower current, when the gap is reduced and it actually follows approximately an exponential growth as shown in the inset using a semilogarithmic scale. The solid line in Fig. 2(c) is a fit with an exponential increase $\exp[-E_g/(2k_BT)]$, where the temperature $T$ is extracted from the Pt resistance [cf. black dots in Fig. 2(d)]. From the fit, we extract the local band gap, $E_g \approx 2$ eV, which is the same as that inferred from the resistivity. The shift of the curve as a function of the gap is consistent with a decrease of the temperature of the detector as the wire is moved away from the injector. One can actually roughly evaluate from this shift the temperature difference in the $x$ direction between the two devices, found to be about 20 °C at $I_B$ when the wires are shifted by 0.3 $\mu$m (difference between the two gaps) along the $x$ axis. We can evaluate quantitatively the expected signal from current leakage through the YIG. At $I = 2.2$ mA, when the temperature of the YIG reaches $T \approx 390$ K, the YIG resistivity drops to about $10^4$ $\Omega$ cm. Considering the equivalent circuit, this will produce a potential difference of 50 $\mu$V on the detector circuit, which is consistent with the observed signal amplitude. This sustains the interpretation that the odd offset voltage in our nonlocal device is purely produced by the decrease of the YIG electrical resistivity. Note that this offset voltage drops very quickly with decreasing current pulse amplitude. As shown in the inset of Fig. 2(c), it decreases by an order of magnitude, when $I = 2.0$ mA (corresponding to a YIG temperature of $T \approx 370$ K). At this level, the offset starts to become of the same order of magnitude as the spin signal in these devices. We have thus indicated by an arrow in Fig. 2(c), $I_B = 2$ mA (i.e., current densities of approximately $10^{12}$ A m$^2$), the threshold current at which the electrical leakage starts to become important in the spin transport experiments, here reaching the 100 nV range.

It is also important to note at this stage that, within our convention of biasing the high/low binding posts of the current source and voltmeter in the same direction [cf. $\oplus$ and $\ominus$ polarities in Fig. 2(a)], the sign of $(V_{\hat{y}|+I} - V_{\hat{y}|-I})/2$ is positive

for positive current and negative for negative current. This is opposite to the sign of the spin conductance, $\Sigma$, reported on these systems (see Ref. [18] or Appendix). The sign of the "odd in $I$" component of the nonlocal voltage is actually a signature that, in one case, the voltage drop is produced by electronic transport (the Ohmic losses) and in the other case, it is produced by spin transport. While in both scenarii the induced electrical current flows in the same direction in the two parallel Pt wires, for Ohmic loss, the YIG acts as an electronic load and the potential drops along the current direction, i.e., $(V_{\hat{y}|+I} - V_{\hat{y}|-I}) \cdot I > 0$ as shown in Fig. 2(c), in contrast, for ISHE, the YIG acts as a spin source for the detector and the potential increases along the current direction, i.e., $\Sigma \cdot I < 0$ as shown in Fig. 4(b) (note that this effect is independent of the sign of the spin Hall angle).

We then move to the even contribution of the offset shown in orange in Fig. 2(d). One observes that this contribution always follows the Joule heating of the Pt wire, so it is linked to the induced thermal gradient. We believe that it should be ascribed to thermoelectric effects produced by temperature gradients along the $y$ direction. This gradient is produced by inherent small resistance asymmetries along the Pt wire length, which results in one end of the Pt wire heating slightly more than the opposite end. This produces a small temperature difference at the two Pt|Al contacts of the detector circuit [indicated by the $\oplus$ and $\ominus$ polarities binding posts in Fig. 2(a)]. Considering the electrical Seebeck coefficient of Pt|Al, of 3.5 $\mu$V/°C [38], the offset measured at $I = 2$ mA, corresponds to a temperature difference of less than 3 °C between the top and bottom contact electrodes, while the wire is being heated by almost 70 °C. These asymmetries in the temperature difference are expected to vary from one device to the other and this is precisely what is observed: the ratio between the even contribution of the offset and the temperature increase of the Pt wire fluctuates and even changes sign randomly between different lateral devices.

## IV. OUT-OF-PLANE OFFSET VOLTAGE IN NONLOCAL YIG|Pt DEVICES: $M_s \parallel \hat{z}$

Although the electrical offset voltage produced by Ohmic losses and thermoelectric effects is independent of the external magnetic field direction when the latter is rotated in-plane, it is in principle sensitive to the out-of-plane component through the Hall effect. Transverse transport properties in YIG are currently attracting a lot of interest and several recent papers address the issue of transverse magnon transport effects in magnetic materials, such as the magnon Hall effect [39] or the magnon planar Hall effect [40]. The sensitivity to magnon effects can be eliminated from the measurements by keeping the magnetization vector in the $yz$ plane containing the interface normal and the length of the Pt stripe as this configuration selects only the transverse transport properties carried by the electrical charge. To extract the Hall voltage, we shall only consider $\Delta_{\hat{z}}$, defined as the difference between the measured voltage for two opposite polarities of the external magnetic field $\pm H_0$, $\Delta_{\hat{z}} = (V_{+\hat{z}} - V_{-\hat{z}})/2$. This signal would be also sensitive to the spin Seebeck effects if the YIG magnetization had a nonvanishing projection along the $x$ axis [18]. The inset of Fig. 3(b) shows the angular dependence as a function

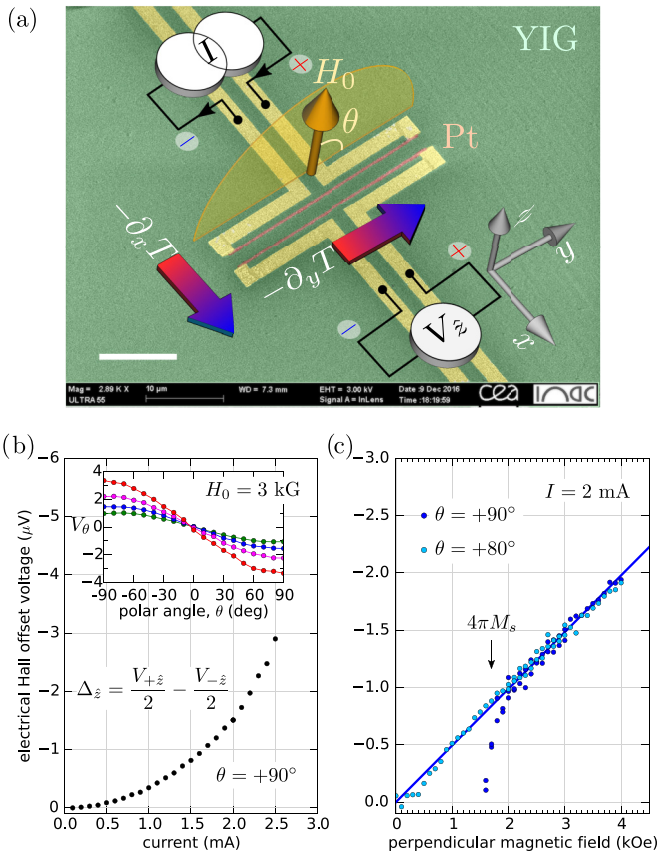


FIG. 3. (a) Schematic of the Righi-Leduc effect produced on a $p$-type conductor magnetized out of plane. The large in-plane temperature gradient $\partial_x T$ produced by Joule heating creates a temperature gradient $\partial_y T$ along the wire when the sample is subject to an out-of-plane magnetic field. (b) Current and (c) magnetic field dependence of the Hall offset voltage $V_{\hat{z}}$ produced in the nonlocal transport device. (a) shows the variation of the $\Delta_{\hat{z}}$ signal as a function of $I$ when $H_0 = \pm 3$ kG. The inset of (b) shows the polar angle variation, $\theta$, for different current between [1.9,2.5] mA (step 0.2 mA). The magnetic field is rotated in the $yz$ plane. (b) shows the magnetic field dependence of $\Delta_{\hat{z}}$ measured when the polar angle reaches the normal direction ($\theta = +90°, +80°$).

of the polar angle, $\theta$, being defined in Fig. 3(a). In all the devices, we observe that the $\theta$ dependence of the $\Delta_{\hat{z}}$ signal is maximum when the field is applied along the $z$ direction, odd in magnetic field, and negative when $\theta = +90°$. Moreover, $\Delta_{\hat{z}}$ increases with both increasing current density and increasing external magnetic field. It is worth to note at this point that the offset voltage produced by the perpendicular magnetic field is about two orders of magnitude smaller than that of the in-plane direction. The observed quadratic dependence with $I$ in Fig. 3(b) suggests that this signal should be associated to Joule heating and thus to particle flux induced by thermal gradients. The observed linear dependence with $H_0$ in Fig. 3(c) suggests that this signal should be associated to a normal Hall effect and not to an anomalous Hall effect linked to $M_s$. Indeed, a fit of the high field data leads to a straight line that intercepts the origin, while the anomalous Hall effect would have led to a finite intercept. One also observes in Fig. 3(c) a

departure from this linear behavior below the saturation field ($\sim 4\pi M_s$). This is because, below saturation, a component of the magnetization could point in the $x$ direction, hereby switching on the sensitivity to the spin Seebeck effect, which is a stronger positive signal in these devices. To check this, we have repeated the measurement by tilting the applied magnetic field by 10° away from the normal and in the $y$ direction ($\theta = 80°$). This ensures that there is no net component along $x$, while retaining almost the same strength along $z$. The result is shown using light blue dots in Fig. 3(b). The fact that the observed linear behavior extends almost up to the origin confirms that the origin of the rise in $\Delta_{\hat{z}}$ is indeed associated to the normal Hall effect.

Next, we discuss more in details the potential origin of the $\Delta_{\hat{z}}$ signal. First, as noted in the previous paragraph, the source is the incoming flux of charge carriers produced by a thermal gradient. This gradient is mainly in the $x$ direction, through the potent Joule heating of the injector. There is in principle an electrical voltage produced in the $y$ direction associated with this incoming flux through the electrical Nernst effect. Our device geometry effectively shunts both contacts with a relatively low impedance Pt wire, acting as a voltage divider, which reduces drastically any sensitivity to the Nernst effect. One should mention at this point the recently reported spin Nernst effect [41]. But this signal should be maximum when the magnetization is parallel to the $y$ direction, while the signal that we discuss here is maximum when the magnetization is parallel to the $z$ direction. We propose here a different scenario to explain our data. Since our measurement of the even offset in Fig. 2(d) seems to indicate that the two thermocouples provided by the Pt|Al contacts at both ends of the detector Pt wire are sensitive to temperature difference along the $y$ direction, the Hall offset signal measured in Fig. 3 can thus be due to a thermal gradient in the $y$ direction (Righi-Leduc effects: a transverse thermal gradient whose amplitude is proportional to the out-of-plane component of the applied magnetic field [42]). Although a definite quantitative proof would require some additional measurements, in the following we shall check that this explanation is consistent with the data.

Firstly, this explanation is consistent with the $I$ and $H_0$ behavior. Secondly, it also has the correct sign. Since the $\Delta_{\hat{z}}$ signal is negative for $\theta = +90°$, this implies that $\partial_x T$ and $\partial_y T$ have the same sign when the field is positive. This is the signature of a $p$-type doping in agreement with Fig. 1(b). Concerning the amplitude of these thermal gradients, at $I_B = 2$ mA, we shall rely on our evaluation of the temperature of the YIG underneath the injector and the detector by measuring the value of the Kittel frequency at these two positions using $\mu$-BLS spectroscopy [cf. inset of Fig. 2(c)]. We found that at $I = 2$ mA the temperature of the YIG increases by $+73\,°\mathrm{C}$ underneath the injector and by $+27\,°\mathrm{C}$ underneath the detector. Using the gap of 0.7 $\mu$m between the two Pt wires as the area where the thermal gradient along $x$ occurs, we find that $\partial_x T = -65\,°\mathrm{C}/\mu\mathrm{m}$. Using a value of $\mu_H = +5\ \mathrm{cm^2\,V^{-1}\,sec^{-1}}$ for the Hall mobility, this would produce a transverse gradient of $\partial_y T = \mu_H H_0 \partial_x T = -1 \times 10^{-2}\,°\mathrm{C}/\mu\mathrm{m}$ in a perpendicular magnetic field of 3 kG. Recalling that the length of the Pt wires is 30 $\mu$m long, this would produce a voltage of 1 $\mu$V, using the thermoelectric coefficient of Pt|Al. So in the end, the expected signal amplitude is of the same order of magnitude as the Hall offset measured at $I_B = 2$ mA.

## V. CONCLUSION

In summary, we have shown that high-quality YIG thin films grown by LPE behave as a large gap semiconductor at high temperature due to the presence of a small amount of impurities inside the YIG. In our case, we observe that the resistivity drops to about $5 \times 10^3\ \Omega\,\mathrm{cm}$ at $T = 400$ K. These results have to be taken into account for nonlocal transport exploring the spin conductivity, especially in cases where the YIG has a large amount of defects like in amorphous materials, or when improper cooling of the sintered product leads to the additional formation of Ohmic grain boundaries. In nonlocal transport devices, these electrical properties are responsible for an offset voltage (independent of the in-plane field direction) whose amplitude, odd in current, grows exponentially with current due to Joule heating. These electrical properties also induce a sensitivity to the perpendicular component of the magnetic field through the Hall effect. In our lateral device, a thermoelectric offset voltage is produced by a temperature gradient along the wire direction proportional to the perpendicular component of the magnetic field (Righi-Leduc effect). These results also emphasize the importance of reducing drastically the Joule heating by using a pulse method, when investigating spin transport in YIG in the strongly out-of-equilibrium regime. For our devices, these electrical effects start to become significant for spin transport studies, when the YIG temperature is heated above 370 K, which corresponds in our case to injecting a current density $> 1.0 \times 10^{12}\ \mathrm{A\,m^2}$ in the Pt (or $I > 2$ mA for these samples). These voltages produced by Ohmic losses in the YIG can be separated from the nonlocal voltage produced by spin transport. Firstly, the two signals have opposite polarities. Secondly, only the latter varies with the orientation of the magnetization in-plane, as first demonstrated by the Gröningen group [13].

## ACKNOWLEDGMENTS

This research was supported by the priority program SPP1538 Spin Caloric Transport (SpinCaT) of the DFG, by FASO of Russia (theme "Spin" No. AAAA-A18-118020290104-2), and by the Russian Ministry of Education and Science (Project No. 14.Z50.31.0025). V.V.N. acknowledges fellowship from the emergence strategic program of UGA, and Russian program of competitive growth of Kazan Federal University.

## APPENDIX A: SPIN CONDUCTANCE IN NONLOCAL YIG|Pt DEVICES: $M_s \parallel \hat{x}$

For the sake of completeness, we display in Fig. 4 the nonlocal spin transport properties produced in the same device by setting the magnetization along the $\hat{x}$ direction. In this configuration, the nonlocal transport of YIG|Pt is dominated by propagating magnons. Since the studied devices are put on a completely different YIG film than the ones reported in Ref. [18], this section illustrates the reproducibility of our findings concerning the spin transport. As explained in

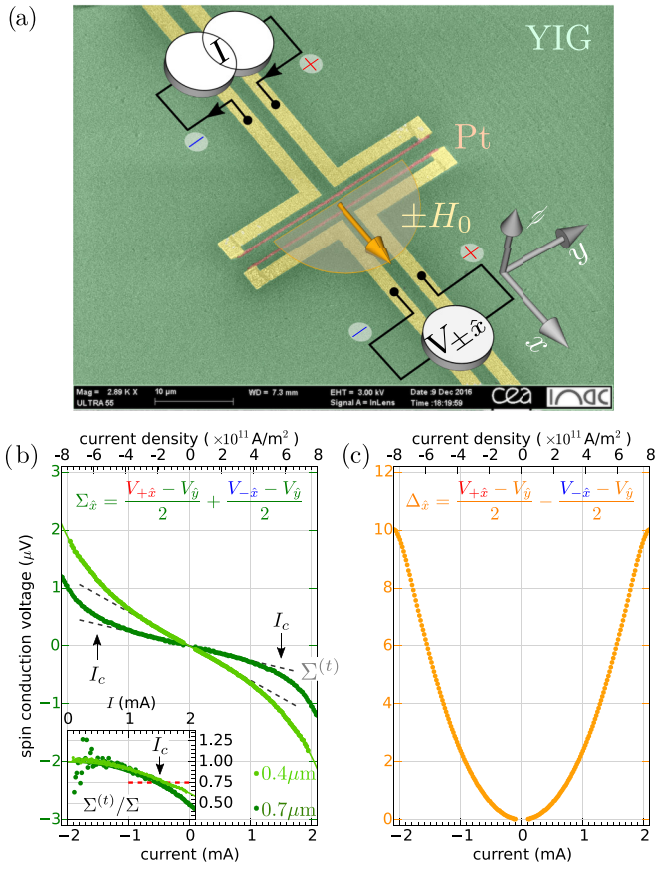


FIG. 4. Nonlocal transport properties observed while applying the external magnetic field in the $\hat{x}$ direction. The transport contribution supported by propagating magnons is extracted by measuring the variation of the nonlocal voltage produced in the $\hat{x}$ direction relative to the nonlocal voltage produced in $\hat{y}$ direction. The measured signal is decomposed in two components: $\Sigma_{\hat{x}}$ (green), the signal sum, and $\Delta_{\hat{x}}$ (orange), the signal difference, respectively, even and odd with respect to the field polarity. (b) and (c) show the current dependence of the amplitude $\Sigma$ and $\Delta$. The dashed line in (b), $\Sigma^{(t)}$, is a linear fit of the low current regime. The inset shows the variation of the normalized inverse spin conductance $\Sigma^{(t)}/\Sigma$ as a function of current. The arrow indicates the crossover current required to observe a 25% change in normalized conductance.

Ref. [18], the magnons transport is isolated by measuring the variation of the nonlocal voltage produced in the $\hat{x}$ direction (ISHE on) relatively to the nonlocal voltage produced in $\hat{y}$ direction (ISHE off). Using the same notation as in Ref. [18], we define the $\Sigma$ voltage as the contribution even with respect to the field polarity and the $\Delta$ voltage as the contribution odd with respect to the field polarity. This is obtained by constructing the signal sum and the signal difference of the nonlocal voltage variation with respect to the field polarity. The result is shown in green in Fig. 4(b) and in orange in Fig. 4(c). As noticed by Cornelissen *et al.* [13], these symmetries of $\Sigma$ and $\Delta$ should be associated respectively to spin-orbit torque [10] and to spin Seebeck effects [43,44]. On these devices too, a deviation from a linear spin conduction transport is observed in Fig. 4(b) at high current. To analyze the value of the crossover to a nonlinear spin transport regime, we repeat the same analysis as the one proposed in Ref. [18]. In the inset of Fig. 4(b), we show the variation of the normalized inverse spin conductance $\Sigma^{(t)}/\Sigma$ as a function of current, where $\Sigma^{(t)}$ is a linear fit of the low current behavior (dashed line). The arrow indicates the current required to observe a 25% change in normalized conductance. The value of the crossover current is $I_c = 1.4$ mA, corresponding to a current density of about $6 \times 10^{11}$A/m$^2$, which is about the same density as the one reported in Ref. [18].

We emphasize again that the polarity of nonlocal voltage produced by spin transport, $\Sigma$, is opposite to the polarity of the nonlocal voltage produced by electrical transport [see Fig. 2(c) and discussion in Sec. III]. The negative value of $\Sigma \cdot I < 0$ reported in Fig. 4(b) is actually an unambiguous signature that the observed nonlocal voltage is produced by ISHE and not by leakage electrical currents inside the YIG [18]. We should though add at this stage that selecting the component of the nonlocal voltage that varies with the in-plane azimuthal angle of the applied magnetic field is another effective mean to eliminate the Ohmic contribution, since the later are independent of the in-plane orientation of $H_0$.

We next discuss the current behavior of $\Delta_{\hat{x}}$ shown in orange in Fig. 4(c). As expected for a signal attributed to thermal effects (spin Seebeck effects), it has the parabolic shape characteristics of Joule heating [cf. black curve in Fig. 2(d)]. It is interesting to note though that the sign of $\Delta_{\hat{x}}$ is opposite to the one reported in Ref. [18]. There have been already several reports on the change of sign of the spin Seebeck coefficient in YIG|Pt devices [13,45–47]. In our case, we report that for all the devices prepared on this thin film (YDPB9) (see Table I), we observe the same opposite sign of $\Delta_{\hat{x}}$ as Ref. [18] independently of the gap value between the two wires (ranging from 0.2 to 6 $\mu$m). We have checked that in these samples the sign of the ISHE signal produced under spin pumping never changes and always remains identical to the polarity reported in Ref. [7]. This rules out potential processes related to the polarization of the top surface, which might have, in the case of a ferrimagnet, opposite magnetization polarization depending on the exact crystallographic surface termination.

## APPENDIX B: PULSE METHOD

An essential earmark of our large power studies on YIG|Pt devices has been the use of a pulse method to measure the nonlocal voltage, as it allows a significant reduction of Joule heating, hereby reducing also the thermal activation of electrical carriers in YIG, when large electrical currents are injected in the Pt wires. In this section, we shall characterize the transient regime associated with the use of current pulses, and we shall describe the practical details on how we have implemented the pulse method in our transport setup.

First, we shall concentrate on the time evolution of the saturation magnetization underneath the injector, when a pulse of electrical current is injected in the Pt wire. These measurements are inferred from time-resolved $\mu$-BLS spectroscopy. To achieve this, we use a current pulse generator that produces a 250-ns-wide current burst, synchronized with the $\mu$-BLS setup. We use this to register the spectrum at different delays. As explained in the main text, one can extract the variation of saturation magnetization produced by Joule heating, $\Delta M_s$, from the shift in the position of the main peak in the $\mu$-BLS spectrum

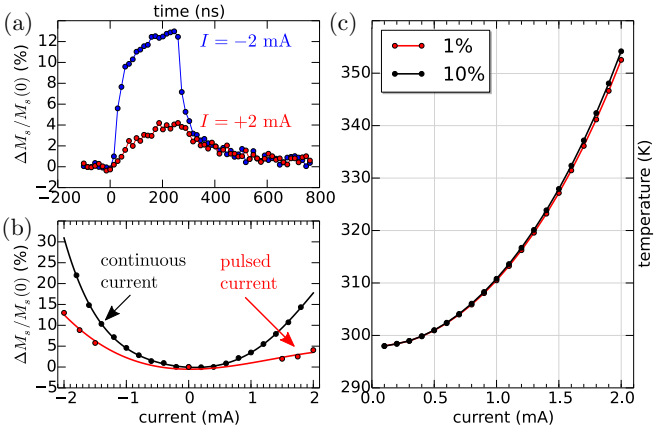


FIG. 5. (a) Temporal evolution of the relative reduction of the saturation magnetization, $\Delta M_s(I)/M_s(0)$, during a current pulse. (b) Current dependence of the maximum obtained in the pulsed- and continuous-current regimes. The data were recorded by placing the probing spot onto the injector Pt stripe. The solid curves are guides for the eye. (c) Variation of the effective temperature of the Pt wire as a function of the duty cycle using the pulse method.

using the Kittel's formula and by assuming that this maximum corresponds to the FMR frequency. The result is shown in Figs. 5(a) and 5(b) for both positive and negative current pulses, while the applied magnetic field is set at $H_0 = 1$ kOe in the $+\hat{x}$ direction. The temporal evolution shows a characteristic rise time of about 200 ns at $I = +2$ mA. It is interesting to note that the variation of the saturation magnetization caused by the current in the Pt stripe shows the same sign for both polarities of the current. This confirms the findings that the total magnon population seems less affected by SOT than the population of small-wave-vector magnons. The possible explanation is that the efficiency of SOT reduces with increasing frequency of magnons because of the increase of their relaxation frequency, while the effects of the Joule heating on the magnon population are expected to be frequency independent. Because of the large phase volume of high-frequency magnons, the total magnon population is then strongly affected by the Joule heating, which counteracts the magnon cooling effect of SOT. This conclusion is further supported by the slow temporal variation of $M_s$ at $I < 0$ [Fig. 5(a)], which can be associated with the slow temperature rise due to the Joule heating. By comparing the data for $I > 0$ and $I < 0$ in Fig. 5(a), one can conclude that, in spite of the large contribution of the heating effects, at least 60% of the detected signal at $I = +2$ mA is due to the magnons excited by SOT. This significant contribution, enabling reliable characterization of the effects of SOT, originates from the small width of the current pulses preventing a significant increase of the temperature of YIG. As seen from the comparison of the current dependencies of $M_s$ obtained in the pulsed- and continuous-current regimes [Fig. 5(b)], utilization of short pulses results in a strong increase of the asymmetry of the measured dependencies reflecting the antisymmetric contribution of SOT.

Next, we shall give the practical details on how we have implemented the pulse method in our transport experiment. For our setup, the current pulses are generated by a 6221 Keithley Current Sources and the induced voltage pulses are measured synchronously by a 2182A Keithley Nanovoltmeter. We use the so-called delta mode (cf. manual), where the induced voltage is calculated through a three-point-average reading, taking into account also the induced voltage before and after the pulse (when $I = 0$). In the Keithleys, the clock is set by the power line cycle (PLC), which has a period of 20 ms in Europe. We chose the width of the pulse duration to be 10 ms and the interval between pulses to be 100 ms (5 PLC), which corresponds to a 10% duty cycle. We have checked that no significant additional heating is generated by the cumulative reading of the voltage with these cycles. Reduction of the duty cycle to 1% shows no significant temperature deviations with the 10% setting when one monitors the variation of the Pt relative resistance as a function of current [see Fig. 5(c)]. In order to avoid the transient regime described above, which might alter the determination of the nonlocal voltage, a 100-$\mu$s delay is applied on the detector voltmeter in order to wait for the stabilization of the voltage before triggering the reading of the nanovoltmeter. For each bias, the nonlocal voltage is calculated from the average of 100 pulses, in order to obtain a tenfold enhancement of the signal to noise ratio. As a precaution, the 20 first pulses are disregarded from the statistics to ensure that a steady-state regime has been reached. In this condition, the deviation of the individual pulse appear to follow a normal distribution around the average, for all pulse amplitude. With these settings, the noise floor obtained is around the 5-nV range for a measurement period of about 10 s.

[1] S. O. Valenzuela and M. Tinkham, Nature (London) **442**, 176 (2006).

[2] Y. Kajiwara, K. Harii, S. Takahashi, J. Ohe, K. Uchida, M. Mizuguchi, H. Umezawa, H. Kawai, K. Ando, K. Takanashi, S. Maekawa, and E. Saitoh, Nature (London) **464**, 262 (2010).

[3] I. M. Miron, K. Garello, G. Gaudin, P.-J. Zermatten, M. V. Costache, S. Auffret, S. Bandiera, B. Rodmacq, A. Schuhl, and P. Gambardella, Nature (London) **476**, 189 (2011).

[4] J.-C. Rojas-Sánchez, L. Vila, G. Desfonds, S. Gambarelli, J. P. Attané, J. M. D. Teresa, C. Magén, and A. Fert, Nat. Commun. **4**, 2944 (2013).

[5] Z. Wang, Y. Sun, M. Wu, V. Tiberkevich, and A. Slavin, Phys. Rev. Lett. **107**, 146602 (2011).

[6] A. V. Chumak, A. A. Serga, M. B. Jungfleisch, R. Neb, D. A. Bozhko, V. S. Tiberkevich, and B. Hillebrands, Appl. Phys. Lett. **100**, 082405 (2012).

[7] C. Hahn, G. de Loubens, O. Klein, M. Viret, V. V. Naletov, and J. Ben Youssef, Phys. Rev. B **87**, 174417 (2013).

[8] O. d'Allivy Kelly, A. Anane, R. Bernard, J. Ben Youssef, C. Hahn, A. H. Molpeceres, C. Carretero, E. Jacquet, C. Deranlot, P. Bortolotti, R. Lebourgeois, J.-C. Mage, G. de Loubens, O. Klein, V. Cros, and A. Fert, Appl. Phys. Lett. **103**, 082408 (2013).

[9] A. Hamadeh, O. d'Allivy Kelly, C. Hahn, H. Meley, R. Bernard, A. H. Molpeceres, V. V. Naletov, M. Viret, A. Anane, V. Cros, S. O. Demokritov, J. L. Prieto, M. Muñoz,

G. de Loubens, and O. Klein, Phys. Rev. Lett. **113**, 197203 (2014).
[10] M. Collet, X. de Milly, O. d'Allivy Kelly, V. Naletov, R. Bernard, P. Bortolotti, J. Ben Youssef, V. Demidov, S. Demokritov, J. Prieto, M. Muñoz, V. Cros, A. Anane, G. de Loubens, and O. Klein, Nat. Commun. **7**, 10377 (2016).
[11] V. Lauer, D. A. Bozhko, T. Brächer, P. Pirro, V. I. Vasyuchka, A. A. Serga, M. B. Jungfleisch, M. Agrawal, Y. V. Kobljanskyj, G. A. Melkov, C. Dubs, B. Hillebrands, and A. V. Chumak, Appl. Phys. Lett. **108**, 012402 (2016).
[12] C. Du, T. van der Sar, T. X. Zhou, P. Upadhyaya, F. Casola, H. Zhang, M. C. Onbasli, C. A. Ross, R. L. Walsworth, Y. Tserkovnyak *et al.*, Science **357**, 195 (2017).
[13] L. J. Cornelissen, J. Liu, R. A. Duine, J. Ben Youssef, and B. J. van Wees, Nat. Phys. **11**, 1022 (2015).
[14] S. T. B. Goennenwein, R. Schlitz, M. Pernpeintner, K. Ganzhorn, M. Althammer, R. Gross, and H. Huebl, Appl. Phys. Lett. **107**, 172405 (2015).
[15] L. J. Cornelissen and B. J. van Wees, Phys. Rev. B **93**, 020403 (2016).
[16] L. J. Cornelissen, K. Oyanagi, T. Kikkawa, Z. Qiu, T. Kuschel, G. E. W. Bauer, B. J. van Wees, and E. Saitoh, Phys. Rev. B **96**, 104441 (2017).
[17] D. Wesenberg, T. Liu, D. Balzar, M. Wu, and B. L. Zink, Nat. Phys. **13**, 987 (2017).
[18] N. Thiery, A. Draveny, V. V. Naletov, L. Vila, J. P. Attané, C. Beigné, G. de Loubens, M. Viret, N. Beaulieu, J. Ben Youssef, V. E. Demidov, S. O. Demokritov, A. N. Slavin, V. S. Tiberkevich, A. Anane, P. Bortolotti, V. Cros, and O. Klein, Phys. Rev. B **97**, 060409 (2018).
[19] C. Safranski, I. Barsukov, H. K. Lee, T. Schneider, A. A. Jara, A. Smith, H. Chang, K. Lenz, J. Lindner, Y. Tserkovnyak *et al.*, Nat. Commun. **8** 117 (2017).
[20] V. Lauer, M. Schneider, T. Meyer, C. Dubs, P. Pirro, T. Brächer, F. Heussner, B. Lägel, V. I. Vasyuchka, A. A. Serga, B. Hillebrands, and A. V. Chumak, arXiv:1612.07305 [cond-mat.mes-hall].
[21] P. K. Larsen and R. Metselaar, Phys. Rev. B **14**, 2520 (1976).
[22] R. Metselaar and P. K. Larsen, *Physics of Magnetic Garnets*, Proceedings of the International School of Physics "Enrico Fermi," edited by A. Paoletti (North-Holland, New York 1978), Vol. 70, p. 417.
[23] H. B. Lal, B. K. Verma, and V. Ram Yadav, J. Mater. Sci. **17**, 3317 (1982).
[24] A. N. Petrov, G. V. Denisov, and V. M. Zhukovskii, Inorg. Mater. (Engl. Transl.) **22**, 4 (1986).
[25] L. Sirdeshmukh, K. Krishna Kumar, S. Bal Laxman, A. Rama Krishna, and G. Sathaiah, Bull. Mater. Sci. **21**, 219 (1998).
[26] K. Modi and P. Sharma, Radiat. Eff. Defects Solids **169**, 723 (2014).
[27] M. Sparks, Phys. Rev. Lett. **22**, 1111 (1969).
[28] Z. Fang, A. Mitra, A. L. Westerman, M. Ali, C. Ciccarelli, O. Cespedes, B. J. Hickey, and A. J. Ferguson, Appl. Phys. Lett. **110**, 092403 (2017).
[29] Y.-M. Kang, S.-H. Wee, S.-I. Baik, S.-G. Min, S.-C. Yu, S.-H. Moon, Y.-W. Kim, and S.-I. Yoo, J. Appl. Phys. **97**, 10A319 (2005).
[30] H. L. Wang, C. H. Du, Y. Pu, R. Adur, P. C. Hammel, and F. Y. Yang, Phys. Rev. B **88**, 100406 (2013).
[31] Y. Sun, Y.-Y. Song, H. Chang, M. Kabatek, M. Jantz, W. Schneider, M. Wu, H. Schultheiss, and A. Hoffmann, Appl. Phys. Lett. **101**, 152405 (2012).
[32] M. C. Onbasli, A. Kehlberger, D. H. Kim, G. Jakob, M. Kläui, A. V. Chumak, B. Hillebrands, and C. A. Ross, APL Mater. **2**, 106102 (2014).
[33] C. Hauser, T. Richter, N. Homonnay, C. Eisenschmidt, M. Qaid, H. Deniz, D. Hesse, M. Sawicki, S. G. Ebbinghaus, and G. Schmidt, Sci. Rep. **6**, 20827 (2016).
[34] C. Dubs, O. Surzhenko, R. Linke, A. Danilewsky, U. Brückner, and J. Dellith, J. Phys. D **50**, 204005 (2017).
[35] L. van der Pauw, Philips Res. Rep. **13**, 1 (1958).
[36] D. C. Bullock and D. J. Epstein, Appl. Phys. Lett. **17**, 199 (1970).
[37] L. J. Cornelissen, K. J. H. Peters, G. E. W. Bauer, R. A. Duine, and B. J. van Wees, Phys. Rev. B **94**, 014412 (2016).
[38] H. Landolt and R. Börnstein, *Group III, Condensed Matter*, Numerical Data and Functional Relationship in Science and Technology (Springer, Berlin, 1970).
[39] Y. Onose, T. Ideue, H. Katsura, Y. Shiomi, N. Nagaosa, and Y. Tokura, Science **329**, 297 (2010).
[40] J. Liu, L. J. Cornelissen, J. Shan, T. Kuschel, and B. J. van Wees, Phys. Rev. B **95**, 140402 (2017).
[41] S. Meyer, Y.-T. Chen, S. Wimmer, M. Althammer, T. Wimmer, R. Schlitz, S. Geprägs, H. Huebl, D. Ködderitzsch, H. Ebert, G. E. W. Bauer, R. Gross *et al.*, Nat. Mater. **16**, 977 (2017).
[42] B. Madon, D. C. Pham, J.-E. Wegrowe, D. Lacour, M. Hehn, V. Polewczyk, A. Anane, and V. Cros, Phys. Rev. B **94**, 144423 (2016).
[43] K. Uchida, J. Xiao, H. Adachi, J. Ohe, S. Takahashi, J. Ieda, T. Ota, Y. Kajiwara, H. Umezawa, H. Kawai, G. E. W. Bauer, S. Maekawa, and E. Saitoh, Nat. Mater. **9**, 894 (2010).
[44] H. Jin, S. R. Boona, Z. Yang, R. C. Myers, and J. P. Heremans, Phys. Rev. B **92**, 054436 (2015).
[45] K. Ganzhorn, T. Wimmer, J. Cramer, R. Schlitz, S. Geprägs, G. Jakob, R. Gross, H. Huebl, M. Kläui, and S. T. B. Goennenwein, AIP Adv. **7**, 085102 (2017).
[46] J. Shan, L. J. Cornelissen, J. Liu, J. Ben Youssef, L. Liang, and B. J. van Wees, Phys. Rev. B **96**, 184427 (2017).
[47] B. L. Giles, Z. Yang, J. S. Jamison, J. M. Gomez-Perez, S. Vélez, L. E. Hueso, F. Casanova, and R. C. Myers, Phys. Rev. B **96**, 180412(R) (2017).